PNAS

www.pnas.org

Supplementary Information for

Societal shifts due to COVID-19 reveal large-scale complexities and feedbacks between atmospheric chemistry and climate change

Joshua L. Laughner, Jessica L. Neu, David Schimel, Paul O. Wennberg, et al.

Full author list:
Joshua L. Laughner, Jessica L. Neu, David Schimel, Paul O. Wennberg, Kelley Barsanti, Kevin Bowman, Abhishek Chatterjee, Bart Croes, Helen Fitzmaurice, Daven Henze, Jinsol Kim, Eric A. Kort, Zhu Liu, Kazuyuki Miyazaki, Alexander J. Turner, Susan Anenberg, Jeremy Avise, Hansen Cao, David Crisp, Joost de Gouw, Annmarie Eldering, John Fyfe, Dan Goldberg, Kevin R. Gurney, Sina Hasheminassab, Francesca Hopkins, Cesunica E. Ivey, Dylan B.A. Jones, Junjie Liu, Nicole S. Lovenduski, Randall V. Martin, Galen A. McKinley, Lesley Ott, Benjamin Poulter, Muye Ru, Stanley P. Sander, Neil Swart, Yuk L. Yung, Zhao-Cheng Zeng, and the rest of the Keck Institute for Space Studies "COVID-19: Identifying Unique Opportunities for Earth System Science" study team

Corresponding Authors:
Joshua L. Laughner: jlaugh@caltech.edu
Jessica L. Neu: jessica.l.neu@jpl.nasa.gov
David Schimel: david.schimel@jpl.nasa.gov, or
Paul O. Wennberg: wennberg@gps.caltech.edu

This PDF file includes:

Supplementary text
Figs. S1 to S11
Tables S1 to S4
References for SI reference citations

Study team author list

The Keck Institute for Space Studies "COVID-19: Identifying Unique Opportunities for Earth System Science" study team includes the following members in addition to the named authors:

- Ron Cohen: University of California Berkeley
- Dan Crichton: Jet Propulsion Laboratory
- John Crounse: California Institute of Technology
- Dan Cusworth: Jet Propulsion Laboratory
- Kevin Donkers: Met Office Informatics Lab (UK)
- Zac Flamig: Amazon
- Joe Flasher: Amazon
- Christian Frankenberg: California Institute of Technology
- Meredith Franklin: University of Southern California
- Randy Friedl: Jet Propulsion Laboratory
- Michael Garay: Jet Propulsion Laboratory
- Chelle Gentemann: Farallon Institute
- Shane Glass: Google
- Kathy Hibbard: National Aeronautics and Space Administration
- Glynn Hulley: Jet Propulsion Laboratory
- Ken Jucks: National Aeronautics and Space Administration
- Olga Kalashnikova: Jet Propulsion Laboratory
- Emma Knowland: National Aeronautics and Space Administration/Goddard Space Flight Center
- Jean-Francois Lamarque: National Center for Atmospheric Research
- Barry Lefer: National Aeronautics and Space Administration
- Chip Miller: Jet Propulsion Laboratory
- Pami Mukherjee: South Coast Air Quality Management District
- Olga Pikelnaya: South Coast Air Quality Management District
- Tom Prince: Keck Institute for Space Studies
- Chris Ruf: Univ. of Michigan
- Natasha Stavros: Jet Propulsion Laboratory
- Britt Stephens: National Center for Atmospheric Research
- Colm Sweeney: National Oceanic and Atmospheric Administration
- Andrew Thorpe: Jet Propulsion Laboratory
- Karin Tuxen-Bettman: Google
- Duane Waliser: Jet Propulsion Laboratory
- Yuan Wang: California Institute of Technology
- Helen Worden: National Center for Atmospheric Research
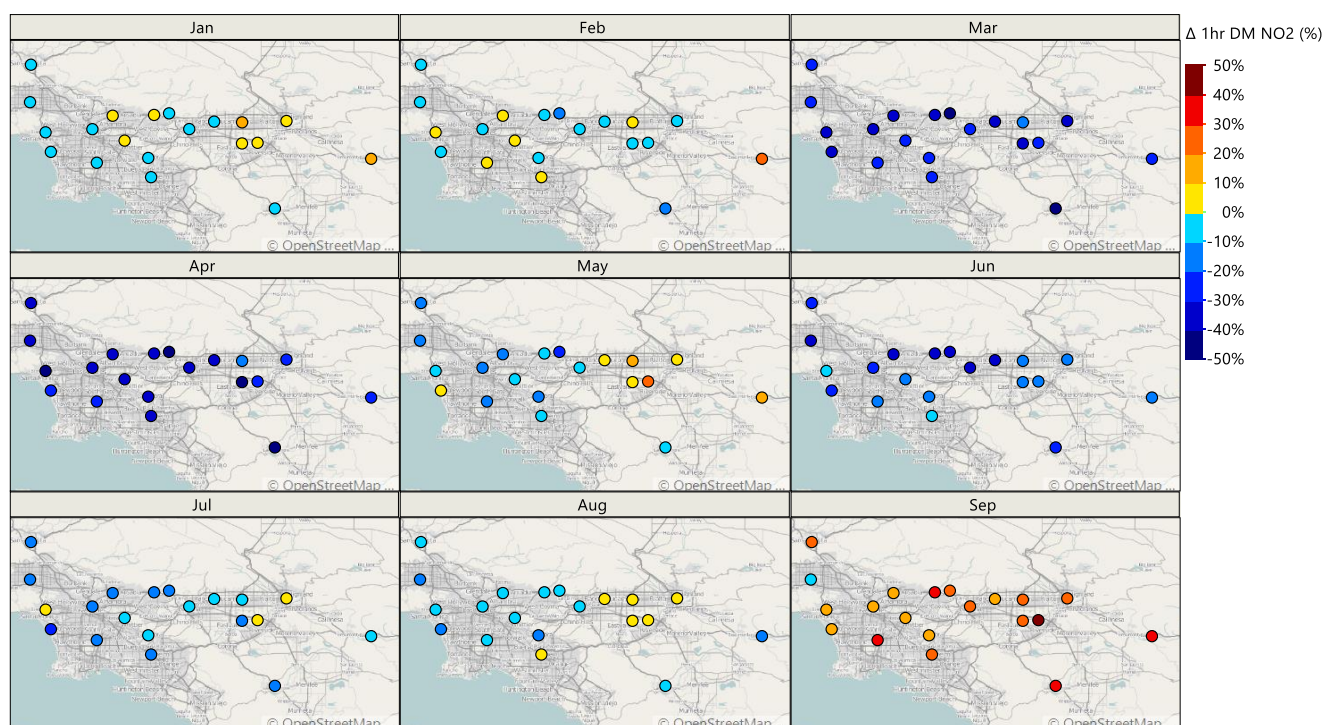- Yuqiang Zhang: Duke University

Joshua L. Laughner, Jessica L. Neu, David Schimel, Paul O. Wennberg, et al.

Additional figures

Fig. S1. Change in 1 hr daily maximum (DM) NO$_2$ in 2020 relative to the average of 2015 to 2019 at the California Air Resources Board sites throughout the South Coast Air Basin.

Fig. S2. Change in 8 hr daily maximum (DM) O$_3$ in 2020 relative to the average of 2015 to 2019 at the California Air Resources Board sites throughout the South Coast Air Basin.
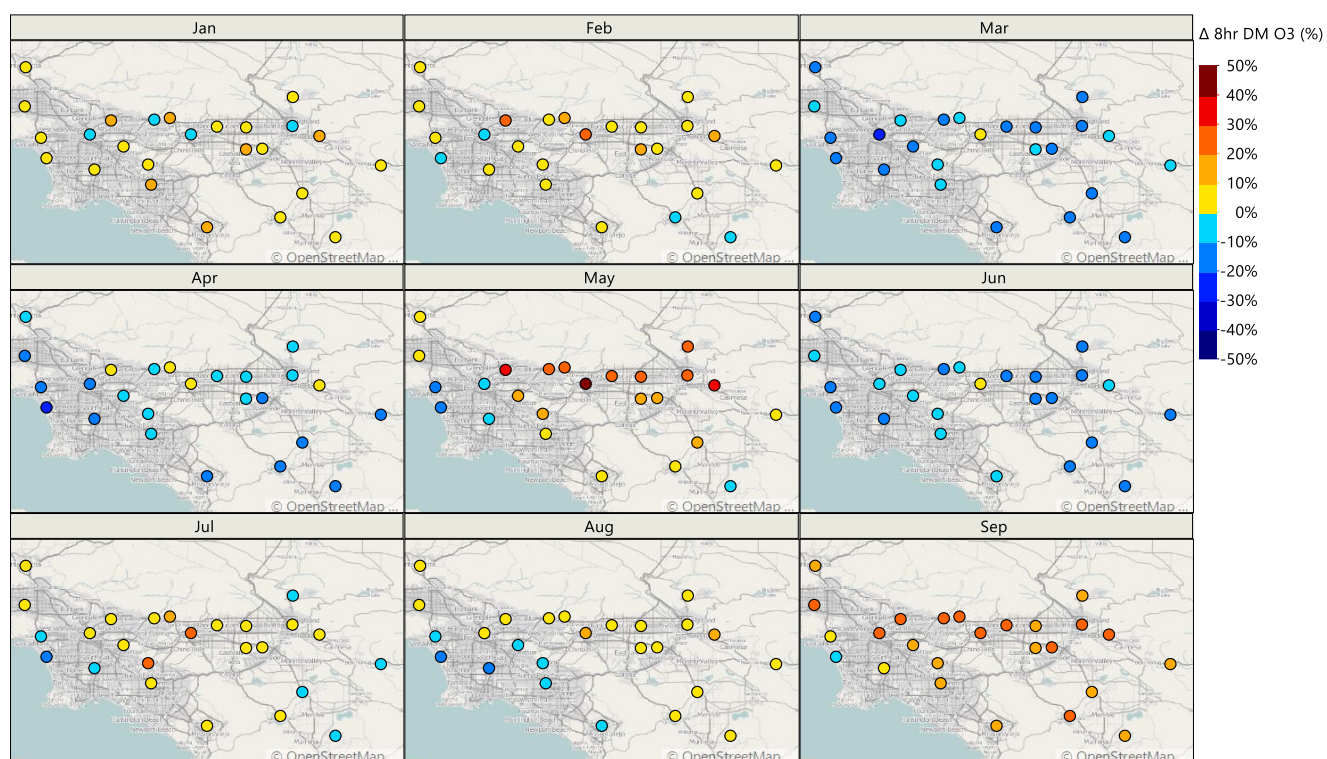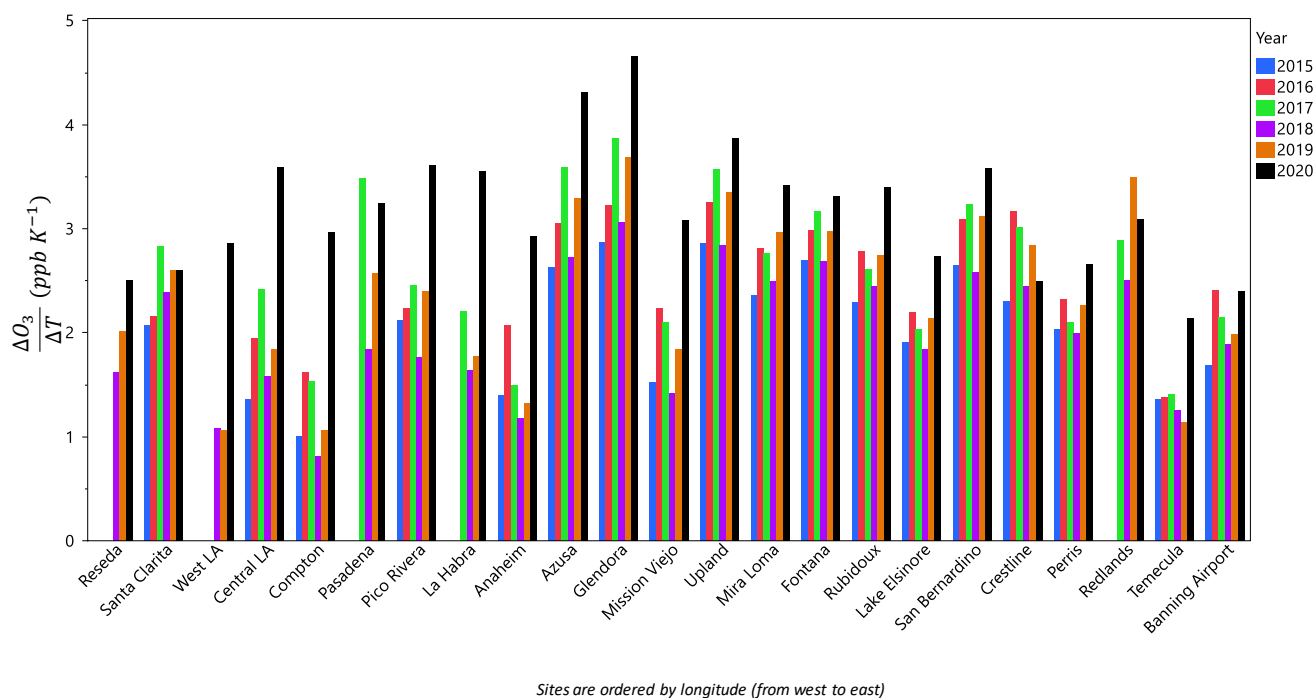
Joshua L. Laughner, Jessica L. Neu, David Schimel, Paul O. Wennberg, et al.

Sites are ordered by longitude (from west to east)

Fig. S3. Average derivatives of O_3 response vs. temperature between May and September at California Air Resources Board sites throughout the South Cost Air Basin for years 2015–2020. Each group of bars is one site, and are ordered by longitude (west to east).
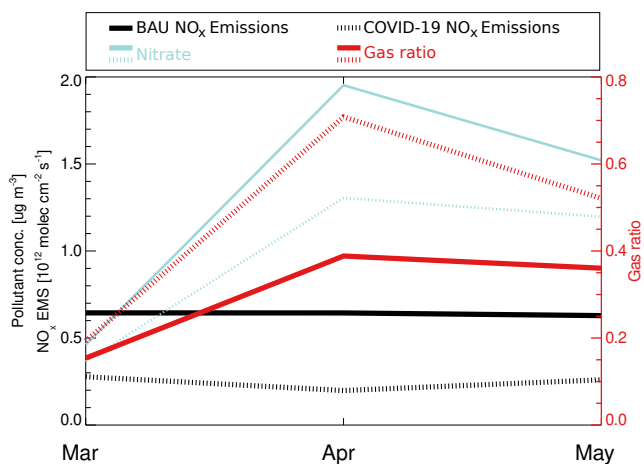

Fig. S4. Simulated inorganic nitrate aerosol sensitivity at downtown LA for two model runs during March to May 2020. Dashed lines represent the run with lockdown-induced emissions reductions (COVID-19), solid lines represent the business as usual (BAU) run. NO_x emissions are shown in black, nitrate aerosol concentration in blue, and the gas ratio in red. A gas ratio < 1 indicates NH_3-limited (compared to NO_x-limited chemistry). See the SI for more information.

Joshua L. Laughner, Jessica L. Neu, David Schimel, Paul O. Wennberg, et al.

Mar: BAU NO$_x$ EMS

Mar: COVID-19 NO$_x$ EMS

Gas ratio

| 0.00 | 0.30 | 0.50 | 0.70 | 0.95 | 1.05 | 1.50 | 2.00 | 3.00 | 10.00 |

Difference (COVID - BAU)

Relative difference (COVID - BAU)/BAU

| -5.0 | -1.0 | -0.5 | -0.1 | 0.1 | 0.5 | 1.0 | 5.0 |

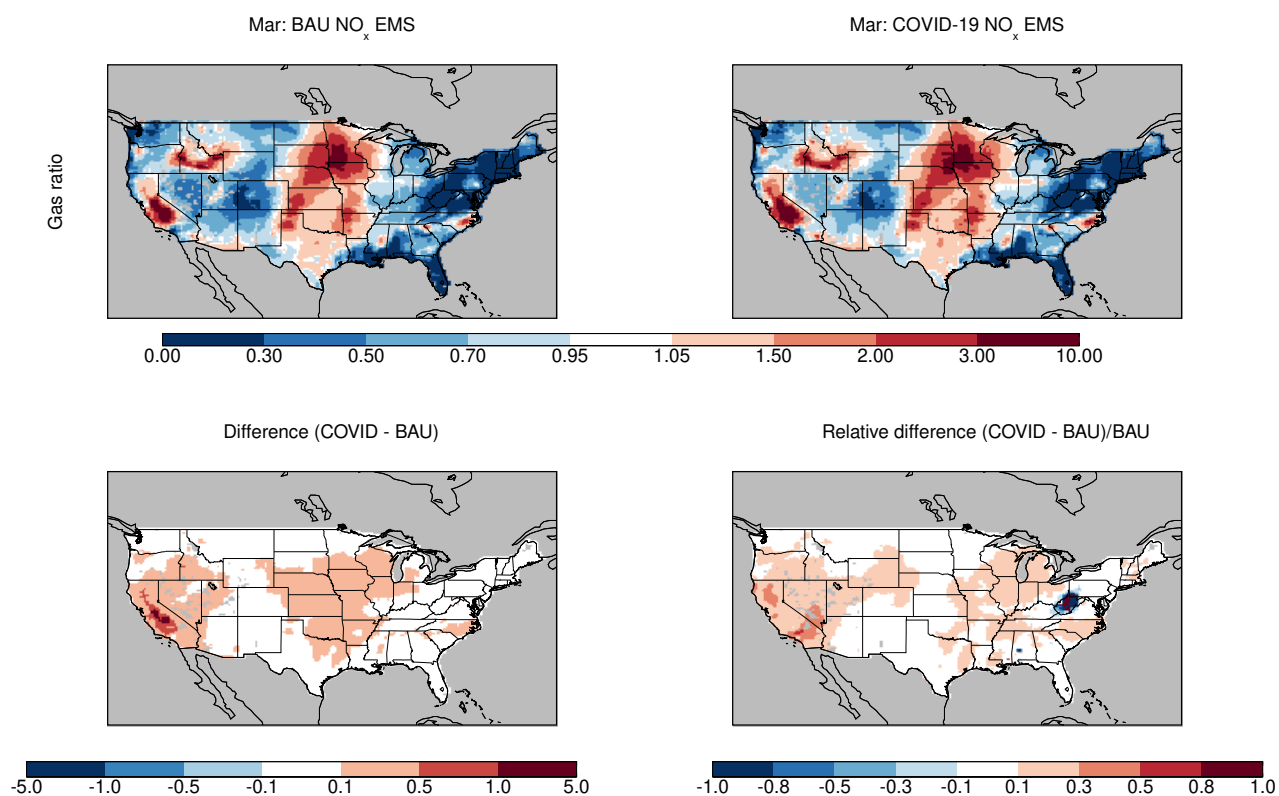| -1.0 | -0.8 | -0.5 | -0.3 | -0.1 | 0.1 | 0.3 | 0.5 | 0.8 | 1.0 |

Fig. S5. Average change in gas ratios for March 2020 between a model simulation using business as usual (BAU) NO$_x$ emissions and one using emissions based on NO$_2$ observations for March 2020 (COVID-19). The gas ratio is described in Eq. (3); a value < 1 indicates NH$_3$ limited nitrate aerosol formation; a value > 1 indicates NO$_x$ limited aerosol formation.
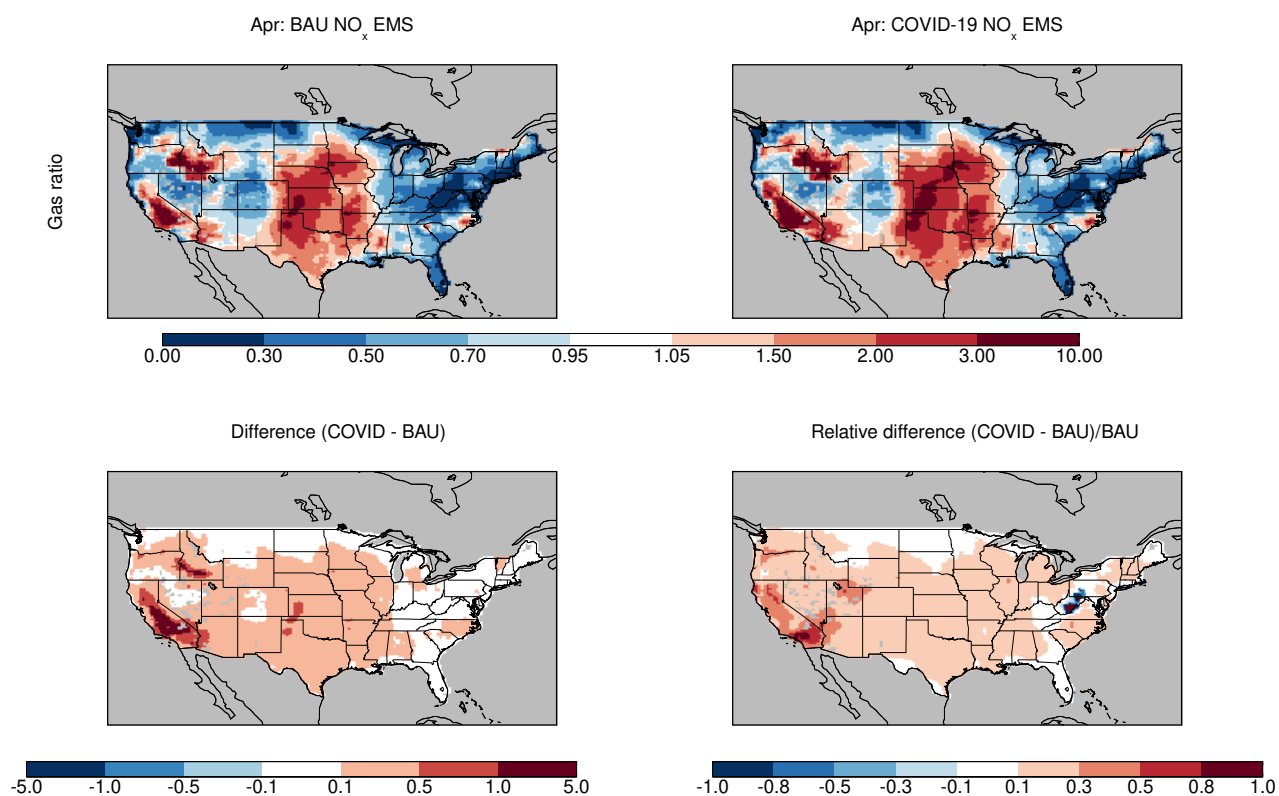
Apr: BAU NO$_x$ EMS

Apr: COVID-19 NO$_x$ EMS

Gas ratio

| 0.00 | 0.30 | 0.50 | 0.70 | 0.95 | 1.05 | 1.50 | 2.00 | 3.00 | 10.00 |

Difference (COVID - BAU)

Relative difference (COVID - BAU)/BAU

| -5.0 | -1.0 | -0.5 | -0.1 | 0.1 | 0.5 | 1.0 | 5.0 |

| -1.0 | -0.8 | -0.5 | -0.3 | -0.1 | 0.1 | 0.3 | 0.5 | 0.8 | 1.0 |

Fig. S6. Same as Fig. S7, but for April 2020.

May: BAU NO$_x$ EMS

May: COVID-19 NO$_x$ EMS

Gas ratio

0.00   0.30   0.50   0.70   0.95   1.05   1.50   2.00   3.00   10.00

Difference (COVID - BAU)

Relative difference (COVID - BAU)/BAU

-5.0   -1.0   -0.5   -0.1   0.1   0.5   1.0   5.0

-1.0   -0.8   -0.5   -0.3   -0.1   0.1   0.3   0.5   0.8   1.0

Fig. S7. Same as Fig. S7, but for May 2020.

Joshua L. Laughner, Jessica L. Neu, David Schimel, Paul O. Wennberg, et al.
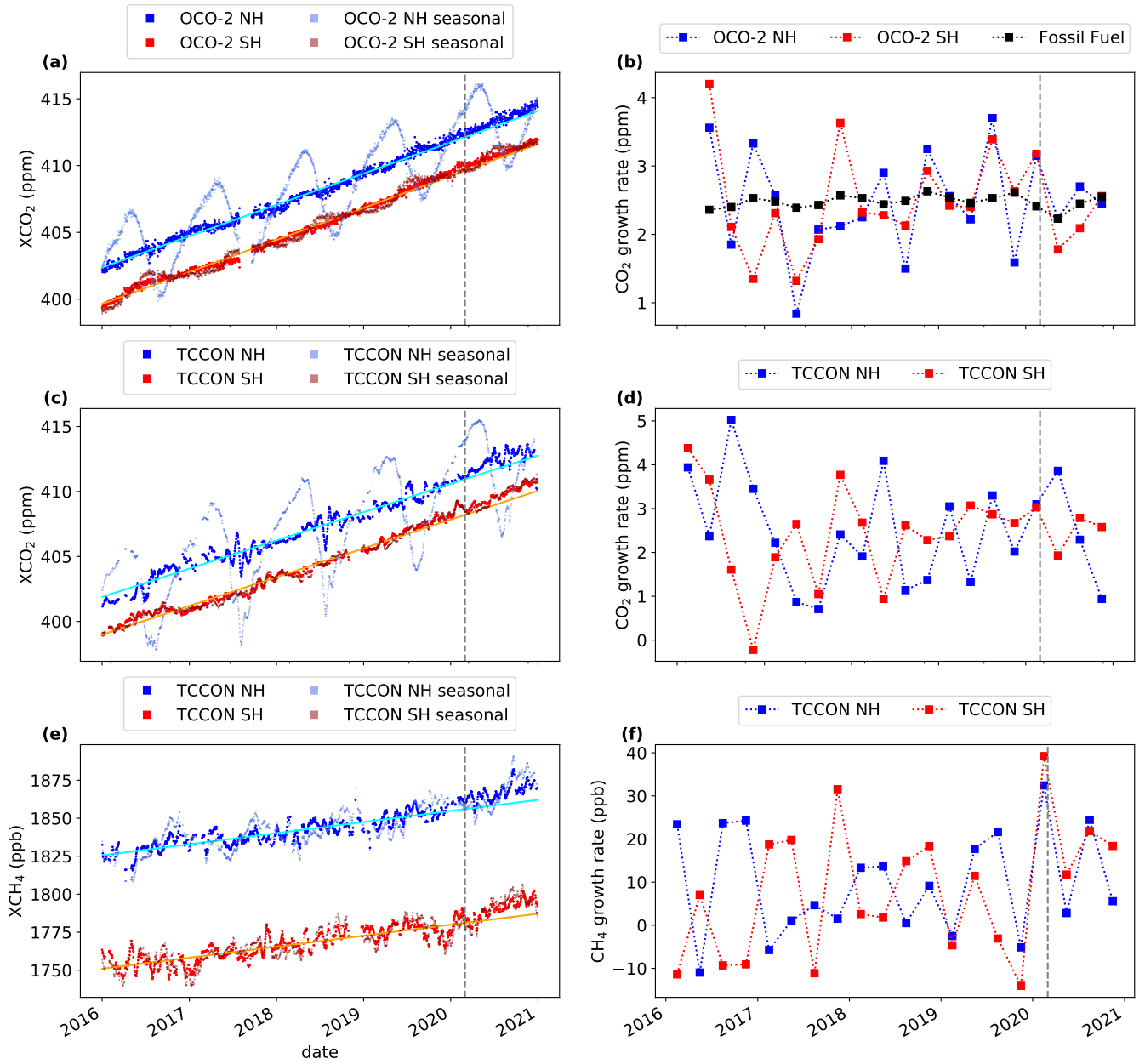
Fig. S8. Trends in column average CO_2 and CH_4. **(a)** Trends in CO_2 from the Orbiting Carbon Observatory 2 (OCO-2) for the northern and southern hemispheres. The pale blue and red markers are daily values, calculated as described in the text. The vibrant blue and red markers represent deseasonalized values computed from the daily values by fitting a fixed seasonal cycle described by a four-term harmonic equation (1, 2). The solid line is a robust linear fit to the 2016 through 2019 data. **(b)** Annual growth rate of CO_2 computed from OCO-2 data in the northern and southern hemispheres, as well as derived from fossil fuel emissions trends. See text for details. **(c)** As (a), but for CO_2 from two Total Carbon Column Observing Network (TCCON) stations: Park Falls, WI, USA in the northen hemisphere and Lauder, New Zealand in the southern hemisphere. **(d)** As (b), but derived from TCCON CO_2. **(e)** As (c), but for CH_4. **(f)** As (d), but for CH_4. In all panels the vertical gray dashed line marks 1 March 2020.
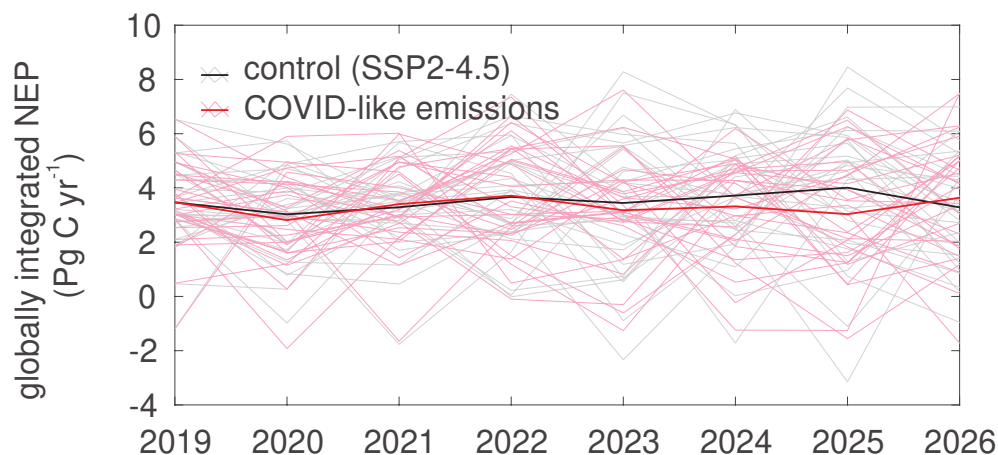
Fig. S9. Annual mean, globally integrated terrestrial net ecosystem production (NEP, positive into biosphere, excludes land use change) predicted from the CanESM5-COVID ensemble (3). As in the main paper, black/gray lines derive from simulations forced with SSP2-RCP4.5 CO_2 emissions, while red/pink lines derive from simulations forced with a 25% peak CO_2 emissions reduction in 2020. See (3) for more details. Thick lines are ensemble averages, and thin lines are individual ensemble members, each with different phasing of internal variability.
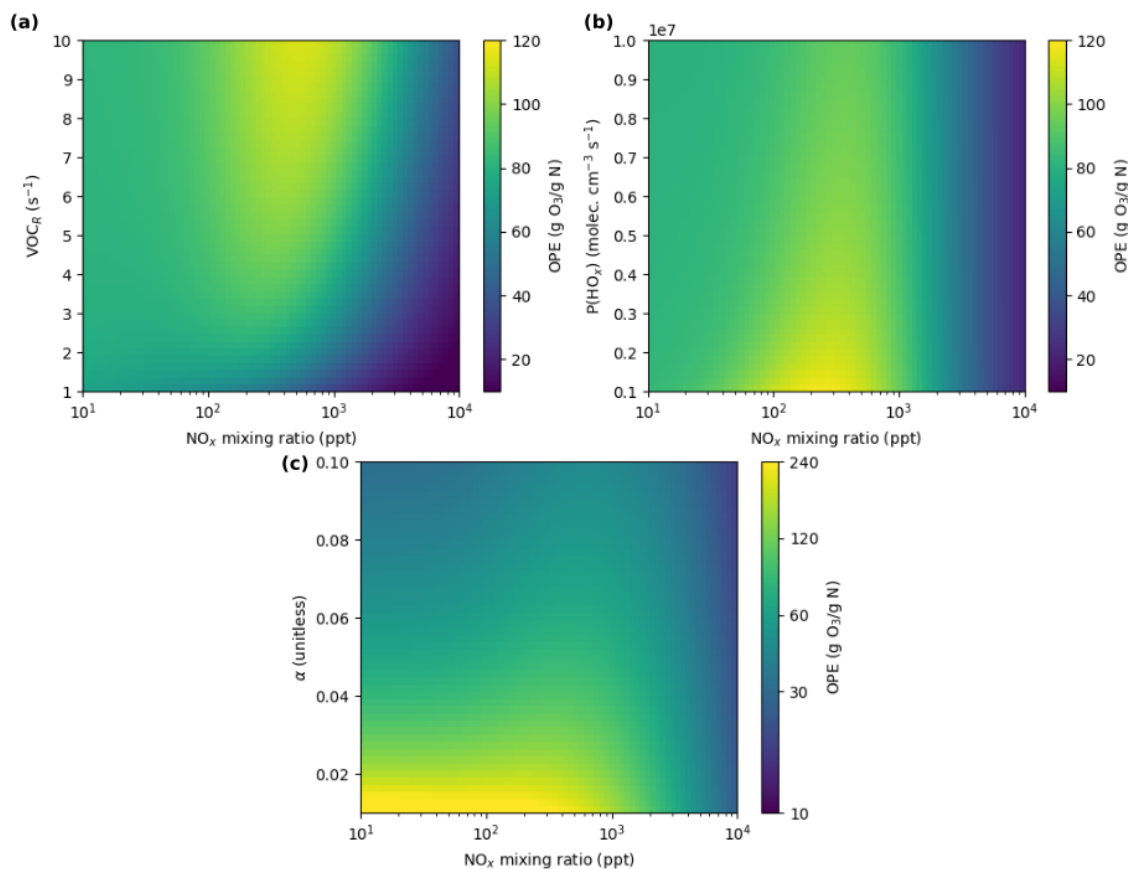

Fig. S10. Theoretical ozone production efficiency as a function of NO_x concentration and one other variable, computed in a steady-state model. In all panels, NO_x concentration is given on the x-axis, the second independent variable on the y-axis, and the color represents the ozone production efficiency. In panel **(a)**, the y-axis is total VOC reactivity, VOC_R; in panel **(b)**, it is total HO_x production, $P(HO_x)$; in panel **(c)**, it is the branching ratio (α) for the $RO_2 + NO$ reaction. Note that the y-axis in panel (b) is multiplied by 10^7 and the color scale for panel (c) has a higher maximum value than the other panels and is logarithmic, rather than linear. The default values for VOC_R, $P(HO_x)$, and α when not the second dependent variables are 5.0 s^{-1}, 6.25×10^6 molec. cm^{-3} s^{-1}, and 0.04, respectively.

Joshua L. Laughner, Jessica L. Neu, David Schimel, Paul O. Wennberg, et al.

Supporting Information Text

Methods

Public data. All public datasets used in this study are shown in Table S1.

Human activity metrics. The human activity metrics in Fig. 2 include the Oxford Coronavirus Government Response Index (4), Opensky-derived flight data (5, 24, 25), Port of LA container moves (https://www.portoflosangeles.org/business/statistics/container-statistics, last accessed 13 May 2021), Port of Long Beach container moves (https://www.polb.com/business/port-statistics/#teus-archive-1995-to-present, last access 20 Feb 2021) Port of Oakland container moves (https://www.oaklandseaport.com/performance/facts-figures/, last accessed 13 May 2021), Caltrans PeMS daily vehicle counts (http://pems.dot.ca.gov/, last accessed 30 Mar 2021), Apple driving mobility data (https://covid19.apple.com/mobility, last accessed 20 Feb 2021), and U.S. Energy Information Agency electricity consumption (https://www.eia.gov/electricity/data/browser/#/topic/, last accessed 20 Feb 2021).

The CAADA Python package (26) was used to preprocess the PeMS vehicle counts and Strohmeier et al. (5) flight data, as well as download Port of LA and Port of Oakland container moves. For the purposes of Fig. 2, "Bay Area" is defined as Alameda, Contra Costa, Marin, San Mateo, San Francisco, Santa Clara, and Santa Cruz counties, while "LA" is defined as Los Angeles, Orange, Riverside, San Bernardino, Santa Barbara, and Ventura counties. For flight data, shipping data, and traffic data, daily values were normalized such that 15 Jan 2020 is 100% and monthly values were normalized such that Jan 2020 was 100%. For electricity use data, each month's value is the 2020 use as a percentage of 2019 use in the same month.

Oxford stringency index: US vs. US state mean. The Oxford Stringency Index (27) includes stringency metrics labeled as US without a subregional code along with metrics for individual states. In Fig. 2, "United States" indicates that the US values without a subregional code are plotted, while "US (state mean)" indicates that the average of all the individual states' stringency indices is plotted. The Oxford index subnational interpretation guide (https://github.com/OxCGRT/covid-policy-tracker/blob/master/documentation/subnational_interpretation.md, last accessed 13 May 2021) indicates that their primary dataset summarizes the totality of policies in the specified territory.

While we include both the combined US and state mean metric to illustrate the general stringency of lockdown measures in the US, we do not ascribe specific meaning to the difference between them.

Equivalent Emissions Year Calculations. For the CO_2 emissions in Fig.3, we used 2005-2018 fossil fuel emissions from the Global Carbon Budget 2019 (28). For 2019, we assumed a +0.1% increase from 2018 based on Supplementary Data in Le Quere et al (29). For 2020 we used a 7% decrease from the 2019 value with a $\pm$ 1% uncertainty, based on Le Quere et al (29) and Liu et al (30). The 2020 emissions are 9.29 ($\pm$ 0.10) GtC/yr; this corresponds to somewhere between 2010 (9.05 GtC/yr) and 2012 (9.50 GtC/yr). For CH_4, we use the anthropogenic emissions based on the EDGARv4.3.2 and GFED4.1s emissions inventories as published in the Global Methane Budget 2000-2017 (31). To estimate the emissions trajectory beyond 2017, we assumed that the rate of increase for 2018 and 2019 was equal to the average rate for 2005 to 2017, then used the estimated 10% reduction in 2020 from (32). For the global NO_x emission trajectory in Fig. 3 we used 2005-2020 emissions from the assimilation system described in the subsection "Global ozone production efficiency calculation" below.

For Fig 9, we again used the NO_x emissions from the assimilation system. For countries whose emissions have been monotonically increasing since 2005, we calculate the prior year with the same emissions as 2020. For countries whose emissions decreased over all or part of the 2005-2019 period, we use the 2015-2019 rate of decline to project emissions into the future.

Global CO_2 emissions estimates. We calculated the daily global fossil CO_2 emissions in 2020 (updated to December 31st), as well as the daily sectoral emissions from power sector, industry sector, transport sector (including ground transport, aviation and shipping), and residential sector respectively. The estimates are based on a set of near real time dataset including hourly to daily electrical power generation data from national electricity operation systems of 31 countries, real-time mobility data (TomTom city congestion index data of 416 cities worldwide and FlightRadar24 individual flight location data), monthly industrial production data (calculated separately by cement production, steel production, chemical production and other industrial production of 27 industries) or indices (primarily Industrial Production Index) from national statistics of 62 countries/regions, and monthly fuel consumption data corrected for the daily population-weighted air temperature in 206 countries.

CO_2 and CH_4 trends and CH_4 box model. CO_2 and CH_4 trends were computed from version 10 column average CO_2 (termed XCO_2) measurements made by the Orbiting Carbon Observatory 2 (OCO-2) satellite instrument and ground based CO_2 and CH_4 column measurements from two Total Carbon Column Observing Network (TCCON) sites: one in Park Falls, WI, USA (45.945° N, 90.273° W) and Lauder, New Zealand (45.038° S, 169.684° E). OCO-2 data was subset to quality flag = 0 data collected in the ocean glint mode and all data averaged daily between 20° N and 55° N for the northern hemisphere and 55° S and 20° S for the southern hemisphere. TCCON data was limited to data with flag = 0; publicly available data is already filtered in this manner.

To compute the trends, 15 day running averages of the daily data were computed and deseasonalized using the method in Liu et al. (1) which follows Graven et al. (2). A robust linear fit was applied to the 2016 through 2019 data. 2020 was excluded so as to test how the 2020 trend compared to the previous four years.

Growth rates were computed from the deseasonalized data by taking the differences in time of three month averages of the OCO-2 or TCCON deseasonalized data, multiplied by four to convert from three-monthly to annual growth rates. The growth

Dataset	Used for	Link	Last access	Citation
Oxford Stringency Index	Human activity metrics	https://www.bsg.ox.ac.uk/research/research-projects/coronavirus-government-response-tracker	20 Feb 2021	(4)
OpenSky-derived flight data	Human activity metrics	https://zenodo.org/record/3928564	31 Mar 2021	(5)
Port of Oakland container moves	Human activity metrics	https://www.oaklandseaport.com/performance/facts-figures/	13 May 2021	
Port of LA container moves	Human activity metrics	https://www.portoflosangeles.org/business/statistics/container-statistics	13 May 2021	
Port of Long Beach container moves	Human activity metrics	https://www.polb.com/business/port-statistics/#teus-archive-1995-to-present	20 Feb 2021	
Caltrans PeMS	Human activity & SF emissions	https://pems.dot.ca.gov/	30 Mar 2021	
Apple mobility trends	Human activity metrics	https://covid19.apple.com/mobility	20 Feb 2021	
US EIA electricity use	Human activity metrics	https://www.eia.gov/electricity/data/browser/#/topic/	20 Feb 2021	
CARB air quality data	LA Basin analysis	https://www.arb.ca.gov/aqmis2/aqdselect.php	11 Nov 2020	
OMI NO_2 columns	Global model assimilation (OPE)	http://www.qa4ecv.eu/ecv/no2-pre/data	11 Nov 2020	(6, 7)
TROPOMI NO_2 columns	Global model assimilation (OPE)	http://www.tropomi.eu/data-products/nitrogen-dioxide	11 Nov 2020	(8)
MOPITT CO	Global model assimilation (OPE)	https://www2.acom.ucar.edu/mopitt	11 Nov 2020	(9)
OMI SO_2 columns	Global model assimilation (OPE)	https://disc.gsfc.nasa.gov/datasets/OMSO2_003/summary	11 Nov 2020	(10, 11)
MLS O_3	Global model assimilation (OPE)	https://mls.jpl.nasa.gov/products/o3_product.php	11 Nov 2020	(12, 13)
MLS HNO_3	Global model assimilation (OPE)	https://mls.jpl.nasa.gov/products/hno3_product.php	11 Nov 2020	(12, 14)
BEACO2N CO_2 data	SF CO_2 emissions estimates	https://beacon.berkeley.edu/	11 Nov 2020	
OCO-2 XCO_2 V10	CO_2 trends	https://ocov2.jpl.nasa.gov/oco-2-data-center/	2 Apr 2021	(15–17)
TCCON CO_2 and CH_4 GGG2014 data	CO_2 & CH_4 trends	https://tccondata.org/	2 Apr 2021	(18–21)
ODIAC	2016–2019 CO_2 emissions for FF growth rate	https://www.odiac.org/index.html	2 Apr 2021	(22)
Carbon Monitor	2020 CO_2 emissions for FF growth rate and 2019/2020 emissions comparison	https://carbonmonitor.org/	2 Apr 2021	(23)
NOAA HRRR meteorology	SF CO_2 emissions estimates	https://rapidrefresh.noaa.gov/hrrr/	11 Nov 2020	
Ocean/land ensemble data	Ocean and land flux responses	http://crd-data-donnees-rdc.ec.gc.ca/CCCMA/publications/COVID19/.	27 May 2021	(3)
GEOS-Chem nitrate simulation	Response of nitrate PM2.5 to NO_x reductions	https://doi.org/10.5281/zenodo.4849416	29 May 2021	

Table S1. Public data sources used in this paper. The "Used for" column gives the part of the analysis in which that data was used.

Joshua L. Laughner, Jessica L. Neu, David Schimel, Paul O. Wennberg, et al.

Year	CO_2 (Gt C/yr)	CH_4 (Tg CH_4/yr)	NO_x (Tg N/yr)
2005	8.02	330.458	36.50
2006	8.29	341.481	37.02
2007	8.54	339.064	36.41
2008	8.73	341.426	36.47
2009	8.61	345.293	34.41
2010	9.05	352.484	36.16
2011	9.35	356.701	36.65
2012	9.50	363.326	35.75
2013	9.54	361.773	35.99
2014	9.61	369.790	37.04
2015	9.62	377.163	35.36
2016	9.66	371.620	33.77
2017	9.77	373.658	34.31
2018	9.98	-	34.30
2019	9.99	-	33.34
2020	9.29	-	30.58

Table S2. Emissions used in Figs. 3 and 9. A dash indicates that emissions data were not available for that year.

rate for fossil fuel emissions was computed by using three month total of anthropogenic CO_2 emissions from the Open-source Data Inventory for Anthropogenic CO_2 (ODIAC) for 2016 through 2019 and carbonmonitor.org for 2020. The three month total emitted CO_2 mass was converted to an atmospheric mixing ratio by:

$$R_{FF} = 4 \cdot E_{CO_2,3mo} \cdot \frac{2.14 \text{ ppm}}{\text{Gt C}} \cdot \overline{f} \qquad [1]$$

where $E_{CO_2,3mo}$ is the three month total CO_2 emissions and $\overline{f}$ is the average airborne fraction computed from all of the OCO-2 data; each three-monthly airborne fraction (f) is computed as:

$$f = \frac{R_{OCO-2,3mo}}{E_{CO_2,3mo} \cdot 2.14 \text{ ppm/Gt C}} \qquad [2]$$

where $R_{OCO-2,3mo}$ is the three-monthly growth rate computed from the OCO-2 data.

The TCCON CH_4 series shown in Fig. 6b are computed from the time series and trends in Fig. 6a. First, the percent difference of the northern and southern hemisphere data against their respective trends is computed. Then, monthly averages of these two percent differences are calculated. Finally, the two monthly time series are averaged together.

The box model trend shown in Fig. 6b was calculated using the box model described in (33) and (34), available at https://github.com/alexjturner/BoxModel_PNAS_20161223. Briefly, this model treats the change in concentration of CH_4 in each hemisphere as the sum of changes due to emissions, oxidation by OH, and interhemispheric transport. OH concentrations can either be directly prescribed or have a prescribed source with concentrations varying alongside CH_4 and CO. The results in Fig. 6b use prescribed OH concentrations, but the behavior is similar if the OH source is prescribed. For simplicity, CH_4 emissions followed the "stabilized" scenario described in (34). The percent difference in CH_4 shown in Fig. 6b is the difference between a model run with a 3% reduction in OH during 2020 and one without.

We do note that, in the box model, the renewed CH_4 growth after 2008 occurs earlier than indicated by in situ measurement. This is due to the timing of CH_4 emissions growth in the EDGAR inventory. However, this does not affect our conclusions as (a) we use the difference of two model runs with the same CH_4 emissions trends and (b) we focus on the behavior in 2020.

TROPOMI NO_2 timeseries. For our analysis we re-grid the operational TROPOMI tropospheric vertical column NO_2, with native pixels of approximately 3.5×7 km^2 for 2019 and 3.5×5.5 km^2 for 2020, to a newly defined $0.01° \times 0.01°$ grid (approximately 1×1 km^2) centered over each of the three cities: Los Angeles, Lima, and Shanghai. Before re-gridding, the data are filtered so as to use only the highest quality measurements (quality assurance flag (QA_flag) > 0.75). By restricting to this QA value, we are removing mostly cloudy scenes (cloud radiance fraction > 0.5) and observations over snow-ice. Once the re-gridding has been completed, the data is binned temporally during a 15-day rolling timeframe and spatially over the metropolitan area, which we loosely define as a $1° \times 1°$ box over the city center. The rolling 75th percentile of the binned data during the first five months of 2019 annd 2020 are shown in top row of Figure 7. There is some evidence that the current TROPOMI operational NO_2 product may have a low bias of 20 to 40% in polluted areas; much of this bias may be attributed to the air mass factor (35–37). We limit our analysis to relative trends, which reduces this uncertainty.

LA Basin AQ analysis. The hourly ambient temperature and concentrations of PM2.5, NO_2, and O_3 in the South Coast Air Basin for the period of 1 Jan 2015 to 30 Sept 2020 were downloaded from the California Air Resources Board Air Quality Data Query Tool (https://www.arb.ca.gov/aqmis2/aqdselect.php). It should be noted that the 2020 data are preliminary, unvalidated, and subject to change. The following steps were taken for data analysis:

1. Only the monitoring sites that had complete data between 2015 and 2020 were considered in this analysis. Near-road monitoring sites were not included in the analysis. Figure S11 and Table S3 show the location of the monitoring sites considered in this analysis and the parameters measured at each site, respectively.

2. For every date and site, the 1hr daily maximum (DM) temperature, 24hr average PM2.5, 1hr DM NO_2, and 8hr average DM O_3 were calculated.

3. For every date, the average of the above-mentioned parameters was calculated across all monitoring sites. 7-day moving averages were then calculated and presented by day of year in Figure 8 for 2020 and the average ($\pm$ range) of [2015-2019]. The background colors in Figure 8 illustrate the difference between the 7-day moving average temperature in 2020 and the average ($\pm 1\sigma$) temperature in [2015-2019] by day of year.

4. Using the data in step 2, the percent change in monthly average concentrations of 1hr DM NO_2 and 8hr DM O_3 between 2020 and the average of [2015-2019] was calculated by month and site as shown in Figures S1 and S2.

Global ozone production efficiency calculation. We evaluated the seasonal and regional changes in the global tropospheric ozone response to COVID-19 NO_x emissions using a state-of-the-art chemical data assimilation system. Anthropogenic NO_x emission reductions linked to the COVID-19 pandemic were estimated as the difference between 2020 emissions and climatological (baseline) emissions for 2010-2019 estimated from our decadal chemical reanalysis constrained by multiple satellite measurements. The assimilation system uses the MIROC-CHASER global chemical transport model and an ensemble Kalman filter technique (38). This approach allows us to capture temporal and spatial variations in transport and chemical
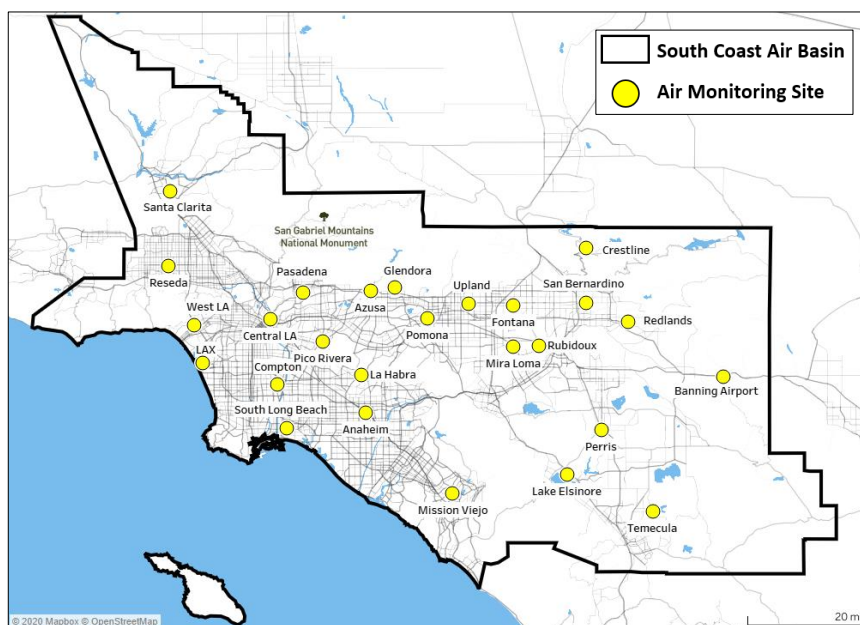
Fig. S11. Location of South Coast Air Basin monitoring sites included in this analysis.

Site	Temperature	O_3	PM2.5	NO_2
Anaheim	✓	✓	✓	✓
Azusa	✓	✓		✓
Banning airport	✓	✓	✓	✓
Central LA	✓	✓	✓	✓
Compton	✓	✓		✓
Crestline	✓	✓	✓	
Fontana	✓	✓		✓
Glendora	✓	✓	✓	✓
La Habra		✓		✓
Lake Elsinore	✓	✓	✓	✓
LAX		✓		✓
Mira Loma	✓	✓	✓	✓
Mission Viejo	✓	✓		
Pasadena		✓		✓
Perris	✓	✓		
Pico Rivera	✓	✓		✓
Pomona		✓		✓
Redlands		✓		
Reseda		✓	✓	✓
Rubidoux	✓	✓	✓	✓
San Bernadino	✓	✓		✓
Santa Clarita	✓	✓	✓	✓
South Long Beach			✓	
Upland	✓	✓	✓	✓
West LA		✓		✓
Temecula	✓	✓	✓	

Table S3. Parameters used from each South Coast Air Basin monitoring site.

Joshua L. Laughner, Jessica L. Neu, David Schimel, Paul O. Wennberg, et al.

reactions in the emission and concentration estimates. The results for 2020 were used previously to evaluate the air quality response to Chinese COVID-19 lockdown (39), and show reasonable agreements with the observed concentrations from in-situ, ozonesonde, and satellite ozone measurements globally for 2005-2018 (39) as well as for 2020 (40).

In order to evaluate seasonal and regional differences in the ozone response, the ozone production efficiency (OPE) was estimated based on model sensitivity calculations using the 2020 and baseline emissions for February-July 2020. The OPE was calculated using the simulated global tropospheric ozone burden changes corresponding to changing NO_x emissions (i.e., the COVID-19 emission anomaly); the analysis was performed separately for each of the selected megacities. The model simulations were conducted from the beginning to the end of each month for the time period February to June, 2020, using the same initial conditions. The simulated tropospheric ozone burden averaged over the last 5 days of each month was compared between the simulations using the 2020 and baseline emissions. The analysis thus provides information on monthly changes in the ozone response (Tg) to reduced NO_x emissions (Tg per year) for each megacity separately. These data are presented in Table S4.

PM2.5 simulations. We used the GEOS-Chem (v9-02) model with a bi-directional NH_3 flux scheme (41) at the nested resolution of $0.3125° \times 0.25°$ latitude to explore the sensitivity of inorganic aerosol formation to NO_x emission reductions in Los Angeles (118.239° W, 34.052° N) during COVID-19. Our detailed O_3-NO_x-VOC-aerosol simulations were driven by Goddard Earth Observing System (GEOS-FP 5.22.0) assimilated meteorological fields and include anthropgenic/biogenic/biomass burning emissions (42–44), gas-phase chemistry (45) and inorganic aerosol partitioning (46), wet/dry depositions (47–49) and transport. We first scaled anthropogenic NO_x and SO_2 emissions from HTAP v2 (42) (originally for the year 2010) to the year 2017 using satellite-derived SO_2 and NO_x emission reduction ratios (50) as our base emissions, which refer to emissions before lockdown during COVID-19. We scaled our base anthropogenic NO_x emissions in March by BAU/COVID monthly NO_x emission ratios from Miyazaki et al. (39) as our BAU/COVID emissions. In the COVID-19 simulations, the NO_x emissions started to decrease on March 1st.

We calculated the gas ratio (51) shown in Fig. S4 using Eq. (3):

$$\text{gas ratio} = \frac{[NH_3] + [NH_4^+] - 2[SO_4^{2-}]}{[HNO_3] + [NO_3^-]} \qquad [3]$$

$[NH_3]$, $[NH_4^+]$, $[SO_4^{2-}]$, $[HNO_3]$ and $[NO_3^-]$ are in units of molar concentrations (mol m^{-3}) and include both gas-phase and aerosol-phase. This gas ratio is an indicator of NH_4NO_3 production sensitivity to NO_x emission change and NH_3 emission change. Values > 1 indicate that NH_4NO_3 production is NO_x limited; values < 1 indicate it is NH_3 limited.

Ozone production efficiency steady state model. The ozone production efficiency (OPE) values in Fig. S10 were computed from a HO_x-NO_x steady state model similar to that used in Laughner et al. (52) (available at https://github.com/joshua-laughner/HSSModel/releases/tag/v0.1.0, an example notebook is available at https://github.com/joshua-laughner/HOx-NOx-model-PNAS-2021). Briefly, this model takes fixed values for NO and NO_2 concentrations, VOC reactivity (VOC_R), HO_x productions ($P(HO_x)$), and RO_2 + NO branching ratio (α) and solves for RO_2, HO_2, and OH concentrations, assuming that HO_2, RO_2, and the whole HO_x family (RO_2 + HO_2 + OH) are in steady state.

Theoretical OPE is computed from the model steady state as the ratio of ozone production to NO_x loss, similar to Kleinman et al. (53) except that formation of alkyl nitrates is counted as NO_x loss:

$$\begin{aligned} OPE_{model} &= \frac{P(O_3)}{L(NO_x)} \\ &= \frac{k_{NO+HO2}[NO][HO_2] + (1-\alpha)k_{NO+RO2}[NO][RO_2]}{k_{NO2+OH}[NO_2][OH] + \alpha k_{NO+RO2}[NO][RO_2]} \end{aligned} \qquad [4]$$

	Country	City	Feb 2020	Mar 2020	Apr 2020	May 2020	Jun 2020
Δ total O_3 (Tg O_3)	China	Shanghai	-0.0159	-0.054	-0.0196	-0.079	-0.1659
	Pakistan	Karachi	-0.0009	-0.0023	-0.0039	0.0031	-0.0069
	India	Mumbai	-0.0075	-0.0067	-0.0077	-0.0053	-0.0538
	China	Beijing	-0.0064	-0.0087	0.0049	0.0033	-0.0227
	Turkey	Istanbul	-0.0032	-0.0136	-0.0041	-0.0151	-0.0353
	China	Guangzhou	-0.0127	-0.02	-0.0164	-0.0281	-0.0277
	India	Delhi	0.0014	0.0096	-0.0268	-0.0152	-0.0313
	Nigeria	Lagos	-0.0186	-0.0336	-0.0532	-0.0912	-0.0594
	South Korea	Seoul	-0.0155	-0.0246	-0.0386	-0.0476	-0.0553
	Brazil	São Paulo	-0.0226	-0.034	-0.0499	-0.039	-0.0308
	Indonesia	Jakarta	0.0043	-0.1095	-0.1149	-0.1084	-0.0961
	Mexico	Mexico City	-0.0221	-0.0376	-0.0817	-0.1191	-0.0879
	Japan	Tokyo	-0.0131	-0.014	-0.0107	-0.0116	-0.019
	United States	New York City	-0.0072	-0.0082	-0.0187	-0.0129	-0.014
	Egypt	Cairo	0.003	-0.0018	-0.0089	-0.0149	-0.0184
	Peru	Lima	-0.0095	-0.0396	-0.0686	-0.0518	-0.0558
	United Kingdom	London	-0.0076	-0.0104	-0.0113	-0.0102	-0.0149
	Iran	Tehran	-0.0141	-0.0105	-0.0442	-0.051	-0.0503
	Australia	Sydney	-0.3071	-0.3481	-0.3528	-0.3601	-0.2905
	United States	Los Angeles	-0.01	-0.02	-0.01	-0.07	-0.11
Δ NO_x emissions (Tg N)	China	Shanghai	-0.553854	-0.646131	-0.245612	-0.359558	-0.396624
	Pakistan	Karachi	0.00108	-0.01083	-0.013907	-0.010837	-0.020179
	India	Mumbai	-0.024593	-0.027663	-0.024419	-0.061499	-0.139134
	China	Beijing	-0.198961	-0.099599	-0.009603	-0.011923	-0.145126
	Turkey	Istanbul	-0.130658	-0.174579	-0.03314	-0.088187	-0.089888
	China	Guangzhou	-0.078471	-0.132469	-0.067583	-0.066167	-0.113306
	India	Delhi	0.013419	0.018727	-0.039327	-0.03435	-0.032617
	Nigeria	Lagos	-0.009639	-0.007365	-0.007956	-0.013574	-0.005402
	South Korea	Seoul	-0.149712	-0.159186	-0.203807	-0.148556	-0.29208
	Brazil	São Paulo	-0.008472	-0.027171	-0.0432	-0.039373	-0.033903
	Indonesia	Jakarta	0.002877	-0.047226	-0.064194	-0.026963	-0.05354
	Mexico	Mexico City	-0.01537	-0.06882	-0.061191	-0.137199	-0.054954
	Japan	Tokyo	-0.041926	-0.034649	-0.029087	-0.039731	-0.059888
	United States	New York City	-0.044813	-0.052346	-0.070999	-0.061666	-0.091085
	Egypt	Cairo	0.024929	-0.012549	-0.023062	-0.04617	-0.050889
	Peru	Lima	-0.002643	-0.01057	-0.015109	-0.017799	-0.020392
	United Kingdom	London	-0.056416	-0.086728	-0.136076	-0.114414	-0.143172
	Iran	Tehran	-0.108269	-0.081617	-0.12622	-0.145247	-0.140058
	Australia	Sydney	-0.122616	-0.090462	-0.125676	-0.177362	-0.151404
	United States	Los Angeles	-0.61	-0.53	-0.19	-0.31	-0.43
OPE (Tg O_3 / Tg N)	China	Shanghai	0.028708	0.083574	0.079801	0.219714	0.41828
	Pakistan	Karachi	-0.833333	0.212373	0.280434	-0.286057	0.34194
	India	Mumbai	0.304965	0.242201	0.315328	0.08618	0.386678
	China	Beijing	0.032167	0.08735	-0.510257	-0.276776	0.156416
	Turkey	Istanbul	0.024491	0.077902	0.123718	0.171227	0.392711
	China	Guangzhou	0.161843	0.150979	0.242665	0.424683	0.244471
	India	Delhi	0.10433	0.512629	0.681466	0.442504	0.959622
	Nigeria	Lagos	1.929661	4.562118	6.686777	6.718727	10.995927
	South Korea	Seoul	0.103532	0.154536	0.189395	0.320418	0.189332
	Brazil	São Paulo	2.667611	1.251334	1.155093	0.990527	0.908474
	Indonesia	Jakarta	1.494612	2.318638	1.789887	4.020324	1.79492
	Mexico	Mexico City	1.437866	0.546353	1.335164	0.868082	1.59952
	Japan	Tokyo	0.312455	0.404052	0.367862	0.291963	0.317259
	United States	New York City	0.160668	0.15665	0.263384	0.209191	0.153703
	Egypt	Cairo	0.120342	0.143438	0.385916	0.32272	0.361571
	Peru	Lima	3.5944	3.746452	4.54034	2.910276	2.736367
	United Kingdom	London	0.134714	0.119915	0.083042	0.08915	0.104071
	Iran	Tehran	0.130231	0.12865	0.350182	0.351126	0.359137
	Australia	Sydney	2.504567	3.848025	2.807219	2.030311	1.918708
	United States	Los Angeles	0.016393	0.037736	0.052632	0.225806	0.255814

Table S4. Changes in NO_x emissions, O_3, and ozone production efficiency inferred from the multi-satellite data assimilation system.

Joshua L. Laughner, Jessica L. Neu, David Schimel, Paul O. Wennberg, et al.

References

1. Liu J, Wennberg PO, Parazoo NC, Yin Y, Frankenberg C (2020) Observational constraints on the response of high-latitude northern forests to warming. *AGU Advances* 1(4).
2. Graven HD, et al. (2013) Enhanced seasonal exchange of CO2 by northern ecosystems since 1960. *Science* 341(6150):1085–1089.
3. Fyfe JC, et al. (2021) Quantifying the influence of short-term emission reductions on climate. *Science Advances* 7(10).
4. Hale T, et al. (2020) Oxford COVID-19 government response tracker. Blavatnik School of Government.
5. Strohmeier M, Olive X, Lübbe J, Schäfer M, Lenders V (2020) Crowdsourced air traffic data from the OpenSky network 2019–20. *Earth System Science Data Discussions* 2020:1–15.
6. Boersma KF, et al. (2017) QA4ECV NO_2 tropospheric and stratospheric column data from OMI. doi: 10.21944/QA4ECV-NO2-OMI-V1.1.
7. Boersma KF, et al. (2018) Improving algorithms and uncertainty estimates for satellite NO_2 retrievals: results from the quality assurance for the essential climate variables (QA4ECV) project. *Atmospheric Measurement Techniques* 11(12):6651–6678.
8. van Geffen J, et al. (2020) S5P TROPOMI NO_2 slant column retrieval: method, stability, uncertainties and comparisons with OMI. *Atmospheric Measurement Techniques* 13(3):1315–1335.
9. Deeter MN, et al. (2017) A climate-scale satellite record for carbon monoxide: the MOPITT Version 7 product. *Atmospheric Measurement Techniques* 10(7):2533–2555.
10. Krotkov NA, et al. (2016) Aura OMI observations of regional SO_2 pollution changes from 2005 to 2015. *Atmospheric Chemistry and Physics* 16(7):4605–4629.
11. Can Li, Nickolay A. Krotkov PL, Joiner J (2020) OMI/Aura Sulphur Dioxide (SO_2) Total Column 1-orbit L2 Swath 13x24 km V003, Greenbelt, MD, USA, Goddard Earth Sciences Data and Information Services Center (GES DISC). Accessed: 11 Nov 2020, doi: 10.5067/Aura/OMI/DATA2022.
12. Livesey NJ, et al. (2018) Earth Observing System (EOS) Aura Microwave Limb Sounder (MLS) Version 4.2x Level 2 and 3 data quality and description document (JPL D-33509 Rev. E). Available from, https://mls.jpl.nasa.gov/data/v4-2_data_quality_document.pdf, last access: 21 Nov 2020.
13. Schwartz M, Froidevaux L, Livesey N, Read W (2015) MLS/Aura Level 2 Ozone (O_3) Mixing Ratio V004, Greenbelt, MD, USA, Goddard Earth Sciences Data and Information Services Center (GES DISC). doi: 10.5067/Aura/MLS/DATA2017.
14. Manney G, Santee M, Froidevaux L, Livesey N, Read W (2015) MLS/Aura Level 2 Nitric Acid (HNO_3) Mixing Ratio V004, Greenbelt, MD, USA, Goddard Earth Sciences Data and Information Services Center (GES DISC). doi: 10.5067/Aura/MLS/DATA2012.
15. Science Data Operations System Jet Propulsion Laboratory (2019) Oco-2 level 2 geolocated XCO2 retrievals results, physical model, retrospective processing v10r.
16. O'Dell CW, et al. (2018) Improved retrievals of carbon dioxide from Orbiting Carbon Observatory-2 with the version 8 ACOS algorithm. *Atmospheric Measurement Techniques* 11(12):6539–6576.
17. Kiel M, et al. (2019) How bias correction goes wrong: measurement of x&ltsub&gtCO&ltsub&gt2&lt/sub&gt&lt/sub&gt affected by erroneous surface pressure estimates. *Atmospheric Measurement Techniques* 12(4):2241–2259.
18. Wunch D, et al. (2015) The Total Carbon Column Observing Network's GGG2014 data version, Technical report.
19. Wennberg PO, et al. (2014) TCCON data from Park Falls (US), Release GGG2014R0 (TCCON data archive, hosted by CaltechDATA).
20. Sherlock V, et al. (2014) TCCON data from Lauder (NZ), 125HR, Release GGG2014R0 (TCCON data archive, hosted by CaltechDATA).
21. Pollard DF, Robinson J, Shiona H (2019) TCCON data from Lauder (NZ), Release GGG2014.R0 (TCCON data archive, hosted by CaltechDATA).
22. Oda T, Maksyutov S, Andres RJ (2018) The open-source data inventory for anthropogenic CO_2, version 2016 (ODIAC2016): a global monthly fossil fuel CO_2 gridded emissions data product for tracer transport simulations and surface flux inversions. *Earth System Science Data* 10(1):87–107.
23. Liu Z, et al. (2021) Global daily CO_2 emissions for the year 2020.
24. Schäfer M, Strohmeier M, Lenders V, Martinovic I, Wilhelm M (2014) Bringing Up OpenSky: A Large-scale ADS-B Sensor Network for Research. *Proceedings of the 13th IEEE/ACM International Symposium on Information Processing in Sensor Networks (IPSN)* pp. 83–94.
25. Olive X (2019) traffic, a toolbox for processing and analysing air traffic data. *Journal of Open Source Software* 4(39).
26. Laughner J (2020) COVID Atmospheric Ancillary Data Agglomerator, v0.1.0.
27. Hale T, et al. (2021) A global panel database of pandemic policies (Oxford COVID-19 government response tracker). *Nature Human Behaviour* 5(4):529–538.
28. Friedlingstein P, et al. (2019) Global carbon budget 2019. *Earth System Science Data* 11(4):1783–1838.
29. Le Quéré C, et al. (2020) Temporary reduction in daily global CO_2 emissions during the COVID-19 forced confinement. *Nature Climate Change* 10(7):647–653.
30. Liu Z, et al. (2020) Near-real-time monitoring of global CO_2 emissions reveals the effects of the COVID-19 pandemic. *Nature Communications* 11(1).
31. Saunois M, et al. (2020) The global methane budget 2000–2017. *Earth System Science Data* 12(3):1561–1623.

32. IEA (2021) Methane tracker 2021 (https://www.iea.org/reports/methane-tracker-2021). last accessed 22 Apr 2021.

33. Turner AJ, Frankenberg C, Wennberg PO, Jacob DJ (2017) Ambiguity in the causes for decadal trends in atmospheric methane and hydroxyl. *Proceedings of the National Academy of Sciences* 114(21):5367–5372.

34. Turner AJ, Frankenberg C, Kort EA (2019) Interpreting contemporary trends in atmospheric methane. *Proceedings of the National Academy of Sciences* 116(8):2805–2813.

35. Griffin D, et al. (2019) High-resolution mapping of nitrogen dioxide with TROPOMI: First results and validation over the Canadian oil sands. *Geophysical Research Letters* 46(2):1049–1060.

36. Judd LM, et al. (2020) Evaluating Sentinel-5P TROPOMI tropospheric NO_2 column densities with airborne and Pandora spectrometers near New York City and Long Island Sound. *Atmospheric Measurement Techniques* 13(11):6113–6140.

37. Verhoelst T, et al. (2020) Ground-based validation of the copernicus Sentinel-5p TROPOMI NO_2 measurements with the NDACC ZSL-DOAS, MAX-DOAS and Pandonia global networks. *Atmospheric Measurement Techniques Discussions* 2020:1–40.

38. Miyazaki K, et al. (2020) Updated tropospheric chemistry reanalysis and emission estimates, TCR-2, for 2005–2018. *Earth System Science Data* 12(3):2223–2259.

39. Miyazaki K, et al. (2020) Air quality response in China linked to the 2019 novel coronavirus (COVID-19) lockdown. *Geophysical Research Letters* 47(19):e2020GL089252. doi: 10.1029/2020GL089252.

40. Miyazaki K, et al. (2021) Global tropospheric ozone responses to reduced NO_x emissions linked to the COVID-19 world-wide lockdowns. *Science Advances* 7(24):eabf7460.

41. Zhu L, et al. (2015) Global evaluation of ammonia bidirectional exchange and livestock diurnal variation schemes. *Atmospheric Chemistry and Physics* 15(22):12823–12843.

42. Janssens-Maenhout G, et al. (2015) HTAP_v2.2: a mosaic of regional and global emission grid maps for 2008 and 2010 to study hemispheric transport of air pollution. *Atmospheric Chemistry and Physics* 15(19):11411–11432.

43. Guenther AB, et al. (2012) The model of emissions of gases and aerosols from nature version 2.1 (MEGAN2.1): an extended and updated framework for modeling biogenic emissions. *Geoscientific Model Development* 5(6):1471–1492.

44. van der Werf GR, et al. (2010) Global fire emissions and the contribution of deforestation, savanna, forest, agricultural, and peat fires (1997–2009). *Atmospheric Chemistry and Physics* 10(23):11707–11735.

45. Mao J, et al. (2010) Chemistry of hydrogen oxide radicals (HO_x) in the arctic troposphere in spring. *Atmospheric Chemistry and Physics* 10(13):5823–5838.

46. Park RJ (2004) Natural and transboundary pollution influences on sulfate-nitrate-ammonium aerosols in the United States: Implications for policy. *Journal of Geophysical Research* 109(D15).

47. Liu H, Jacob DJ, Bey I, Yantosca RM (2001) Constraints from ^{210}Pb and ^{7}Be on wet deposition and transport in a global three-dimensional chemical tracer model driven by assimilated meteorological fields. *Journal of Geophysical Research: Atmospheres* 106(D11):12109–12128.

48. Wang Q, et al. (2011) Sources of carbonaceous aerosols and deposited black carbon in the arctic in winter-spring: implications for radiative forcing. *Atmospheric Chemistry and Physics* 11(23):12453–12473.

49. Amos HM, et al. (2012) Gas-particle partitioning of atmospheric Hg(II) and its effect on global mercury deposition. *Atmospheric Chemistry and Physics* 12(1):591–603.

50. Miyazaki K, et al. (2019) Chemical reanalysis products, doi: 10.25966/9qgv-fe81.

51. Ansari AS, Pandis SN (1998) Response of inorganic PM to precursor concentrations. *Environmental Science & Technology* 32(18):2706–2714.

52. Laughner JL, Cohen RC (2019) Direct observation of changing NO_x lifetime in North American cities. *Science* 366(6466):723–727.

53. Kleinman LI, et al. (2002) Ozone production efficiency in an urban area. *Journal of Geophysical Research: Atmospheres* 107(D23):ACH 23–1–ACH 23–12.